

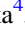



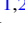
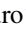


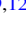
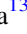
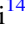
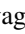
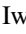
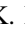
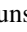

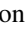

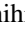

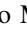
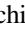

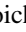


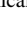
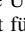
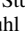
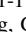
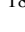





# Subaru High- $z$ Exploration of Low-luminosity Quasars (SHELLQs). XII. Extended [C II] Structure (Merger or Outflow) in a $z = 6.72$ Red Quasar

Takuma Izumi<sup>1,2,31</sup> , Masafusa Onoue<sup>3</sup> , Yoshiki Matsuoka<sup>4</sup> , Michael A. Strauss<sup>5</sup> , Seiji Fujimoto<sup>6,7</sup> , Hideki Umehata<sup>8,9</sup> , Masatoshi Imanishi<sup>1,2</sup> , Taiki Kawamuro<sup>1</sup> , Tohru Nagao<sup>4</sup> , Yoshiki Toba<sup>4,10,11</sup> , Kotaro Kohno<sup>9,12</sup> , Nobunari Kashikawa<sup>13</sup> , Kohei Inayoshi<sup>14</sup> , Toshihiro Kawaguchi<sup>15</sup> , Kazushi Iwasawa<sup>16</sup> , Akio K. Inoue<sup>17,18</sup> , Tomotsugu Goto<sup>19</sup> , Shunsuke Baba<sup>1</sup> , Malte Schramm<sup>20</sup> , Hyewon Suh<sup>21,22</sup> , Yuichi Harikane<sup>23</sup> , Yoshihiro Ueda<sup>10</sup> , John D. Silverman<sup>13,24</sup> , Takuya Hashimoto<sup>25</sup> , Yasuhiro Hashimoto<sup>26</sup> , Soh Ikarashi<sup>27</sup> , Daisuke Iono<sup>1,2</sup> , Chien-Hsiu Lee<sup>28</sup> , Kianhong Lee<sup>9</sup> , Takeo Minezaki<sup>9</sup> , Kouichiro Nakanishi<sup>1,2</sup> , Suzuka Nakano<sup>2</sup> , Yoichi Tamura<sup>29</sup> , and Ji-Jia Tang<sup>30</sup> 

<sup>1</sup> National Astronomical Observatory of Japan, 2-21-1 Osawa, Mitaka, Tokyo 181-8588, Japan; [takuma.izumi@nao.ac.jp](mailto:takuma.izumi@nao.ac.jp)

<sup>2</sup> Department of Astronomical Science, The Graduate University for Advanced Studies, SOKENDAI, 2-21-1 Osawa, Mitaka, Tokyo 181-8588, Japan

<sup>3</sup> Max-Planck-Institut für Astronomie, Königstuhl 17, D-69117 Heidelberg, Germany

<sup>4</sup> Research Center for Space and Cosmic Evolution, Ehime University, 2-5 Bunkyo-cho, Matsuyama, Ehime 790-8577, Japan

<sup>5</sup> Princeton University Observatory, Peyton Hall, Princeton, NJ 08544, USA

<sup>6</sup> Cosmic Dawn Center, Copenhagen, Denmark

<sup>7</sup> Niels Bohr Institute, University of Copenhagen, Lyngbyvej 2, DK-2100 Copenhagen, Denmark

<sup>8</sup> RIKEN Cluster for Pioneering Research, 2-1 Hirosawa, Wako, Saitama 351-0198, Japan

<sup>9</sup> Institute of Astronomy, Graduate School of Science, The University of Tokyo, 2-21-1 Osawa, Mitaka, Tokyo 181-0015, Japan

<sup>10</sup> Department of Astronomy, Kyoto University, Kitashirakawa-Oiwake-cho, Sakyo-ku, Kyoto 606-8502, Japan

<sup>11</sup> Academia Sinica Institute of Astronomy and Astrophysics, 11F Astronomy-Mathematics Building, AS/NTU, No. 1, Section 4, Roosevelt Road, Taipei 10617, Taiwan

<sup>12</sup> Research Center for the Early Universe, Graduate School of Science, The University of Tokyo, 7-3-1 Hongo, Bunkyo-ku, Tokyo 113-0033, Japan

<sup>13</sup> Department of Astronomy, School of Science, The University of Tokyo, 7-3-1 Hongo, Bunkyo-ku, Tokyo 113-0033, Japan

<sup>14</sup> Kavli Institute for Astronomy and Astrophysics, Peking University, Beijing 100871, People's Republic of China

<sup>15</sup> Department of Economics, Management and Information Science, Onomichi City University, 1600-2, Hisayamada, Onomichi, Hiroshima, 722-8506, Japan

<sup>16</sup> ICREA and Institut de Ciències del Cosmos, Universitat de Barcelona, IEEC-UB, Martí i Franquès, 1, E-08028 Barcelona, Spain

<sup>17</sup> Department of Physics, School of Advanced Science and Engineering, Faculty of Science and Engineering, Waseda University, 3-4-1, Okubo, Shinjuku, Tokyo 169-8555, Japan

<sup>18</sup> Waseda Research Institute for Science and Engineering, Faculty of Science and Engineering, Waseda University, 3-4-1, Okubo, Shinjuku, Tokyo 169-8555, Japan

<sup>19</sup> Institute of Astronomy and Department of Physics, National Tsing Hua University, Hsinchu 30013, Taiwan

<sup>20</sup> Graduate School of Science and Engineering, Saitama University, 255 Shimo-Okubo, Sakura-ku, Saitama City, Saitama 338-8570, Japan

<sup>21</sup> Subaru Telescope, National Astronomical Observatory of Japan, 650 North Aohoku Place, Hilo, HI 96720, USA

<sup>22</sup> Gemini Observatory/NSF's NOIRLab, 670 North Aohoku Place, Hilo, HI 96720, USA

<sup>23</sup> Institute for Cosmic Ray Research, The University of Tokyo, 5-1-5 Kashiwanoha, Kashiwa, Chiba 277-8582, Japan

<sup>24</sup> Kavli Institute for the Physics and Mathematics of the Universe (WPI), The University of Tokyo Institutes for Advanced Study, The University of Tokyo, 5-1-5 Kashiwanoha, Kashiwa, Chiba 277-8583, Japan

<sup>25</sup> Tomonaga Center for the History of the Universe, Faculty of Pure and Applied Sciences, University of Tsukuba, Tsukuba, Ibaraki 305-8571, Japan

<sup>26</sup> Department of Earth Sciences, National Taiwan Normal University, Taipei 11677, Taiwan

<sup>27</sup> Centre for Extragalactic Astronomy, Department of Physics, Durham University, South Road, Durham DH1 3LE, UK

<sup>28</sup> NSF's National Optical-Infrared Astronomy Research Laboratory, 950 North Cherry Avenue, Tucson, AZ 85719, USA

<sup>29</sup> Division of Particle and Astrophysical Science, Graduate School of Science, Nagoya University, Furo-cho, Chikusa-ku, Nagoya, Aichi 464-8602, Japan

<sup>30</sup> Research School of Astronomy and Astrophysics, Australian National University, Cotter Road, Weston Creek, ACT 2611, Australia

Received 2020 October 23; revised 2020 December 29; accepted 2020 December 30; published 2021 February 26

## Abstract

We present Atacama Large Millimeter/submillimeter Array [C II] 158  $\mu\text{m}$  line and far-infrared (FIR) continuum emission observations toward HSC J120505.09–000027.9 (J1205–0000) at  $z = 6.72$  with a beam size of  $\sim 0''.8 \times 0''.5$  (or  $4.1 \text{ kpc} \times 2.6 \text{ kpc}$ ), the most distant red quasar known to date. Red quasars are modestly reddened by dust and are thought to be in rapid transition from an obscured starburst to an unobscured normal quasar, driven by powerful active galactic nucleus (AGN) feedback that blows out a cocoon of interstellar medium. The FIR continuum of J1205–0000 is bright, with an estimated luminosity of  $L_{\text{FIR}} \sim 3 \times 10^{12} L_{\odot}$ . The [C II] line emission is extended on scales of  $r \sim 5 \text{ kpc}$ , greater than that of the FIR continuum. The line profiles at the extended regions are complex and broad (FWHM  $\sim 630\text{--}780 \text{ km s}^{-1}$ ). Although it is not practical to identify the nature of this extended structure, possible explanations include (i) companion/merging galaxies and (ii) massive AGN-driven outflows. For the case of (i), the companions are modestly star-forming ( $\sim 10 M_{\odot} \text{ yr}^{-1}$ ) but are not detected by our Subaru optical observations ( $y_{\text{AB},5\sigma} = 24.4 \text{ mag}$ ). For the case of (ii), our lower limit to the cold neutral outflow rate is  $\sim 100 M_{\odot} \text{ yr}^{-1}$ . The outflow kinetic energy and momentum are both much lower than predicted in energy-conserving wind models, suggesting that the AGN feedback in this quasar is not capable of completely suppressing its star formation.

*Unified Astronomy Thesaurus concepts:* AGN host galaxies (2017); Active galactic nuclei (16); Quasars (1319); Submillimeter astronomy (1647); Galaxy evolution (594); Galaxy formation (595); High-redshift galaxies (734)

<sup>31</sup> NAOJ Fellow.

## 1. Introduction

It has long been considered that the mergers or interactions of gas-rich galaxies are the trigger for intense starbursts and black hole growth (e.g., Sanders et al. 1988; Hopkins et al. 2006). In this scenario, a substantial fraction of the black hole growth takes place inside a dusty starburst, during which time the system appears as an obscured active galactic nucleus (AGN; Hickox & Alexander 2018). Subsequent strong AGN feedback, particularly in the form of massive outflows (e.g., Maiolino et al. 2012; Cicone et al. 2014; Carniani et al. 2016; Bischetti et al. 2019; Fluetsch et al. 2019; Lutz et al. 2020), is expected to clear gas and dust from the galaxy, halting further star formation and black hole growth. This feedback is also invoked in galaxy evolution models to shape the galaxy mass function and ultimately black hole–host galaxy coevolution relations (Kormendy & Ho 2013).

High-redshift quasars are a unique laboratory in which to test or refine our understanding of early supermassive black hole (SMBH) and galaxy formation (e.g., Inayoshi et al. 2020). To date,  $>200$  quasars with absolute ultraviolet (UV) magnitudes  $M_{1450} \lesssim -22$  are known at  $z > 5.7$ , most of which were discovered by wide-field optical and near-infrared surveys (e.g., Fan et al. 2001; Bañados et al. 2016; Matsuoka et al. 2016, 2018a, 2018b). Submillimeter/millimeter observations have revealed that their host galaxies often possess copious amounts of dust ( $\sim 10^8 M_\odot$ ) and gas ( $\sim 10^{10} M_\odot$ ) with high star formation rates (SFRs) of  $\gtrsim 100\text{--}1000 M_\odot \text{ yr}^{-1}$  (e.g., Wang et al. 2013; Venemans et al. 2016, 2017; Decarli et al. 2018), while smaller values are found in lower-luminosity quasars (e.g., Willott et al. 2013, 2015, 2017; Izumi et al. 2018, 2019).

As galaxy overdensity increases the likelihood of interactions and mergers of galaxies, deep submillimeter searches for companion star-forming galaxies have been performed toward  $z \gtrsim 6$  quasars mainly by using the Atacama Large Millimeter/submillimeter Array (ALMA). Such efforts have tried to detect the  $C^+ \ ^2P_{3/2} \rightarrow \ ^2P_{1/2}$   $157.74 \mu\text{m}$  (hereafter [C II]  $158 \mu\text{m}$ ) line and/or rest-frame far-infrared (FIR) continuum emission from companions. Indeed, some works have found companions (e.g., Decarli et al. 2017; Trakhtenbrot et al. 2017; Willott et al. 2017; Neeleman et al. 2019), or very close, likely merging galaxies (Bañados et al. 2019; Decarli et al. 2019; Venemans et al. 2019), to optically luminous ( $M_{1450} \lesssim -26$  mag) quasars, which would support the triggering of quasars by gas-rich major mergers. In contrast to this, no overdensity of submillimeter continuum emitters has been reported for the case of optically less luminous ( $M_{1450} \gtrsim -25$  mag) quasars (Izumi et al. 2019), implying that rather secular processes (e.g., Shirakata et al. 2019; Marshall et al. 2020) may also be capable of triggering  $z \gtrsim 6$  quasars.

As massive quiescent galaxies already exist at  $z \sim 3\text{--}4$  (e.g., Straatman et al. 2014; Estrada-Carpenter et al. 2020), we also anticipate that AGN feedback is already taking place at higher redshift. An outstanding case is the  $z = 6.42$  quasar J1148+5251, in which a massive AGN-driven outflow (outflow rate  $\dot{M}_{\text{out}} > 1400 M_\odot \text{ yr}^{-1}$ ) extending to  $r > 10$  kpc is detected in the [C II]  $158 \mu\text{m}$  emission line (Maiolino et al. 2012; Cicone et al. 2015). However, there is no other single  $z > 6$  quasar in which [C II] outflow has been reported, likely due to inadequate sensitivity. To overcome the sensitivity issue, Bischetti et al. (2019) stacked the [C II] cubes of 48 quasars at  $4.5 < z < 7.1$  and reported a successful detection of a broad [C II] wing: the inferred outflow rate ( $\dot{M}_{\text{out}} \sim 100 M_\odot \text{ yr}^{-1}$ ) is only modest, but may be enough to quench star formation in the central regions

of these galaxies. On the other hand, Novak et al. (2020) performed another stacking analysis of [C II] cubes of 27  $z \gtrsim 6$  quasars, revealing no clear evidence of [C II] outflows (see also Decarli et al. 2018). Hence the situation is quite controversial these days. In either case, however, previous  $z \gtrsim 6$  studies are biased toward the unobscured (= blue) quasar population.

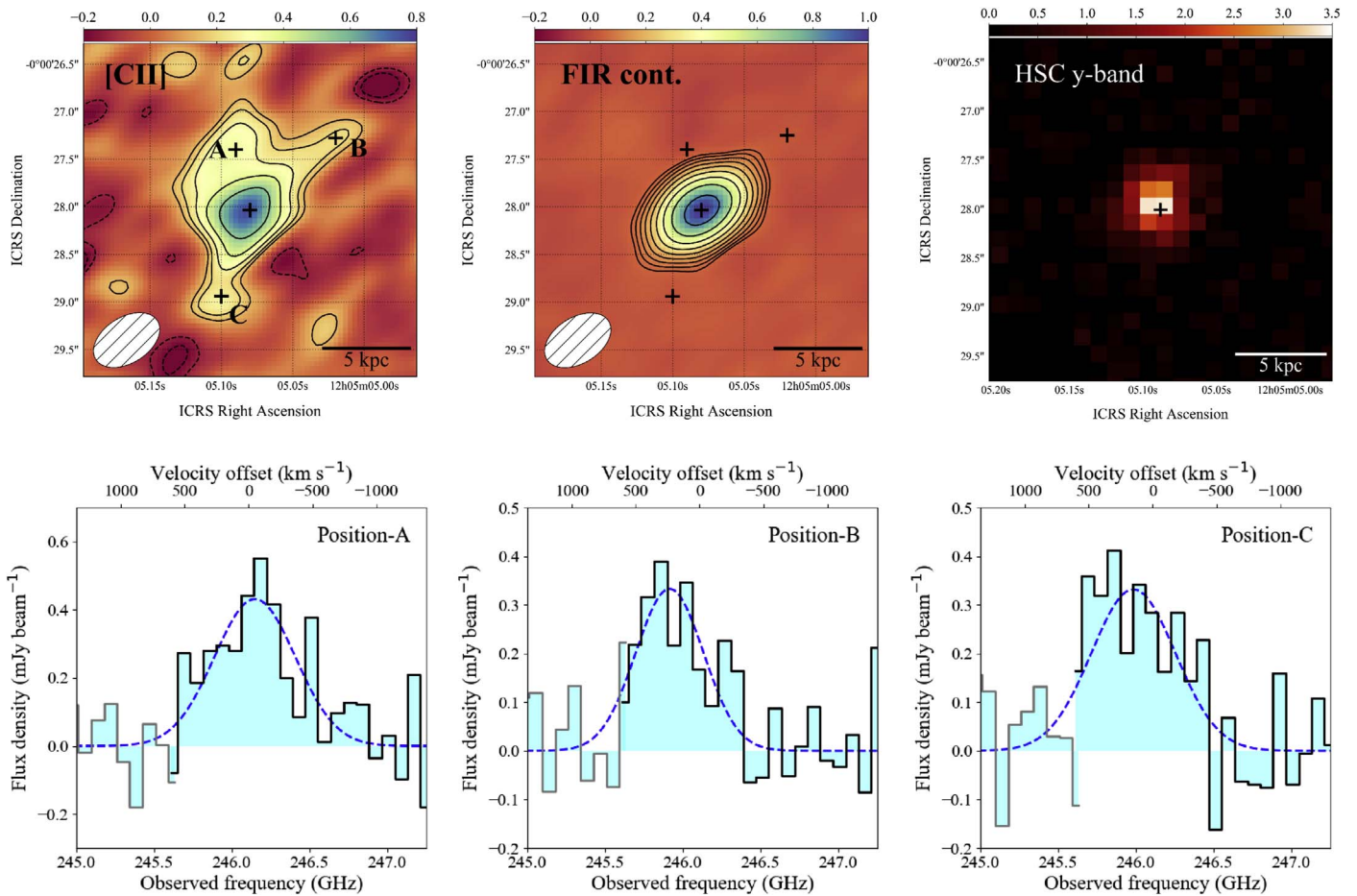
In this regard, one intriguing population of quasars, whose host galaxies have not been studied at all at  $z > 6$ , is the so-called *red quasars*. Unlike the unobscured population, they are reddened ( $E(B - V) > 0.1$ ) by dust at the rest-UV (e.g., Richards et al. 2003; Glikman et al. 2004, 2018; Ross et al. 2015). Red quasars typically have high Eddington ratios and are accompanied by broad absorption line (BAL) features indicative of nuclear fast outflows (e.g., Richards et al. 2003; Urrutia et al. 2009). At lower redshifts like  $z \lesssim 2.5$ , red quasars often host galaxy-scale outflows at various gas phases (e.g., Brusa et al. 2018; Perrotta et al. 2019; Zakamska et al. 2019). In addition, high-resolution imaging observations have revealed that red quasars tend to be hosted by major mergers (e.g., Urrutia et al. 2008; Glikman et al. 2015). These properties support an evolutionary scenario in which red quasars emerge from the merger-induced dusty starburst phase likely by blowing out the surrounding medium with powerful winds (e.g., Farrah et al. 2012). However, as no red quasar has been identified at  $z > 5$  primarily due to its apparent faintness in the rest-UV, it is not clear if this picture also holds in the first generation of quasars.

### 1.1. Our Target: J1205–0000

Very recently, we successfully discovered two red quasars at  $z > 5.8$  (Kato et al. 2020) by matching the deep sample of quasars optically selected from the Subaru Hyper Suprime-Cam (HSC) wide-field survey (Aihara et al. 2018) with mid-infrared photometric data obtained by the Wide-field Infrared Survey Explorer (WISE). In this work, we present our ALMA observations of the [C II]  $158 \mu\text{m}$  line and underlying FIR continuum emission of one of these two sources, J120505.09–000027.9 (hereafter J1205–0000; Figure 1 top right) at  $z = 6.7$ , by far the highest-redshift red quasar known (Kato et al. 2020).<sup>32</sup> Without correcting for dust extinction, J1205–0000 has a rest-frame UV magnitude of  $M_{1450} = -24.4$  mag (Matsuoka et al. 2016). But once extinction ( $E(B - V) = 0.12$  mag) is accounted for, the quasar has  $M_{1450} = -26.1$  mag, with an Eddington ratio of 0.22 (Kato et al. 2020); here the reddening was estimated by fitting a typical quasar template to the broadband (optical to mid-infrared) spectral energy distribution with the Small Magellanic Cloud dust extinction law. J1205–0000 hosts prominent NV and CIV BALs as well, confirming the existence of nuclear outflows (Onoue et al. 2019).

In the following parts, we describe the ALMA observations in Section 2, the extended nature of the [C II] emission in Section 3, and the possible origins of the extended structures in Section 4. We provide our conclusions in Section 5. This is the twelfth in a series of publications presenting the results from our high-redshift quasar survey, the Subaru High- $z$  Exploration of Low-luminosity Quasars. Throughout this work, we adopt the standard cosmology with  $H_0 = 70 \text{ km s}^{-1} \text{ Mpc}^{-1}$ ,  $\Omega_M = 0.3$ , and  $\Omega_\Lambda = 0.7$ .

<sup>32</sup> Mazzucchelli et al. (2017) performed submillimeter observations toward this quasar by using the NOEMA interferometer but did not detect [C II] emission as the line was out of their frequency coverage.



**Figure 1.** (Top left) Integrated [C II] 158  $\mu\text{m}$  intensity map of J1205–0000 ( $\text{Jy beam}^{-1} \text{ km s}^{-1}$  units). We integrated over a velocity range of  $\pm 500 \text{ km s}^{-1}$  relative to the systemic redshift ( $z_{[\text{C II}]}$  = 6.7224), which was determined from a double Gaussian fit to the area-integrated spectrum (Figure 3(b)). Contours start at  $\pm 3\sigma$  ( $1\sigma = 0.045 \text{ Jy beam}^{-1} \text{ km s}^{-1}$ ) and increase in powers of  $\sqrt{2}$ . The synthesized beam is shown in the corner. The central black plus denotes the continuum peak position. Three representative positions with which to extract the off-center spectrum are marked A, B, and C. (Top middle) Spatial distribution of the rest-FIR continuum emission ( $\text{mJy beam}^{-1}$  units). Contours again start at  $\pm 3\sigma$  ( $1\sigma = 17.6 \mu\text{Jy beam}^{-1}$ ) and increase in powers of  $\sqrt{2}$ . The same off-center positions (A–C) are marked. (Top right) Subaru HSC  $y$ -band map of the same region (arbitrary units), shown as a reference of the optical light distribution of J1205–0000. (Bottom panels) The [C II] 158  $\mu\text{m}$  spectra extracted at the three different off-center positions (A–C) with the synthesized beam. The velocities are relative to the systemic redshifts. The results of a single Gaussian fit to these spectra are shown in Table 1.

## 2. ALMA Observations

We observed the redshifted [C II] line and FIR continuum emission of J1205–0000 in Band 6 on 2020 February 26 (ID = 2019.1.00074.S; principal investigator: T. Izumi), with 41 antennas. Our observations were conducted in a single pointing with a  $24''$  diameter field of view. The baseline length ranged from 15.1 to 783.5 m, resulting in a maximum recoverable scale of  $\sim 6''$ . J1256–0547 was observed as a flux and bandpass calibrator, and J1217–0029 was monitored to calibrate the complex gain. The total on-source time was 71 minutes.

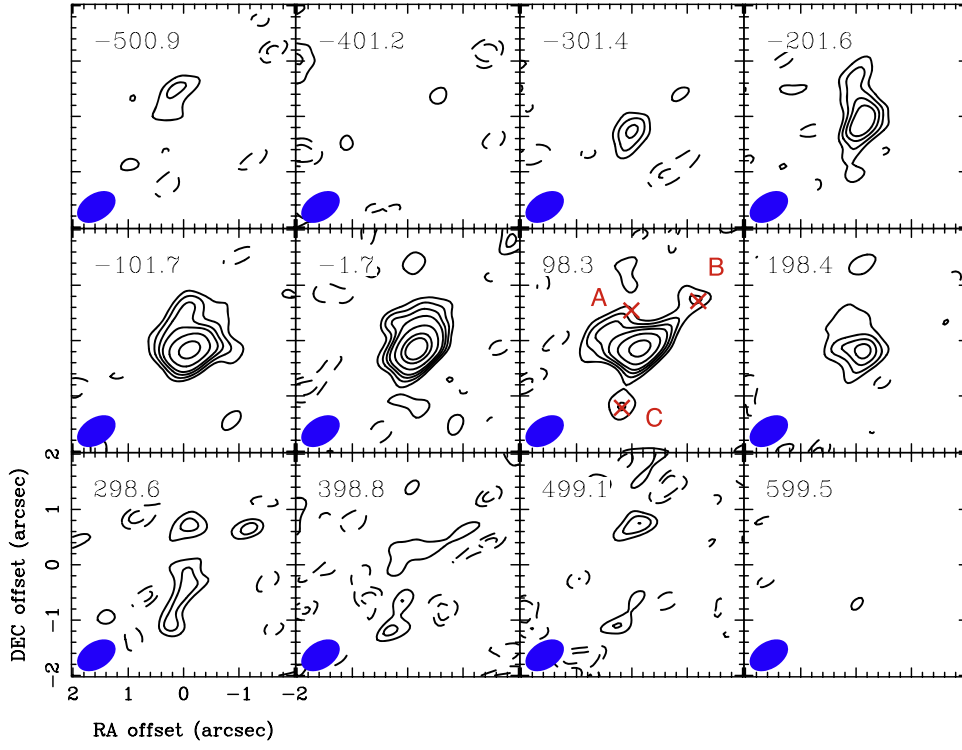
The data were processed using CASA version 5.6 (<https://casa.nrao.edu>). All images were reconstructed with the `tclean` task using natural weighting to maximize sensitivity. We averaged several channels to obtain a velocity resolution of  $100 \text{ km s}^{-1}$ , which resulted in a  $1\sigma$  channel sensitivity of  $0.13 \text{ mJy beam}^{-1}$  (beam size =  $0''.77 \times 0''.48$ , P.A. =  $-58^\circ$ ). Note that we first cleaned the line cube including the continuum emission down to the  $3\sigma$  level to determine the line position. With this knowledge, we identified the channels free of line emission. All these line-free channels were integrated to generate a continuum map ( $1\sigma = 17.6 \mu\text{Jy beam}^{-1}$ ), which was

subtracted in the  $uv$  plane by using the first-order polynomial before making the final line cube.

Throughout the paper, only statistical errors are displayed unless mentioned otherwise (absolute flux uncertainty of  $\sim 10\%$ ; ALMA Cycle 7 Proposer’s Guide). As the [C II] emission turned out to fall at around the edge of one of the spectral windows, we display spectral data from two contiguous windows when necessary. We also used the MIRIAD software (Sault et al. 1995) for some of the analyses in this paper.

## 3. Result: Extended [C II] Emission

The top panels of Figure 1 show the distributions of the velocity-integrated [C II] 158  $\mu\text{m}$  line emission and FIR continuum emission. An optical  $y$ -band image of J1205–0000 taken with the Subaru HSC is also shown for reference. Figure 2 shows the [C II] channel maps revealing the global velocity structure. We describe the details of this emission in the following subsections. The relevant physical properties are summarized in Table 1.



**Figure 2.** Velocity channel maps of [C II] line emission of J1205–0000. Each channel is labeled with its central velocity in kilometers per second. The plus signs indicate the FIR continuum peak position. The three representative off-center positions (Figure 1) are also marked at the 98 km s<sup>−1</sup> channel. The synthesized beam is plotted in the bottom left corner. Contours are drawn at the  $-3$  and  $-2\sigma$  levels (dashed line) and at the 2, 3, 4, 5, 7, 10, 12, and  $15\sigma$  levels (solid line;  $1\sigma = 0.13$  mJy beam<sup>−1</sup>). Extended emission exists at several off-center positions over several contiguous channels.

**Table 1**  
Observed and Derived Properties of J1205–0000

	Area-integrated [C II] 158 $\mu$ m Line Emission		
	Single Gaussian	Double Gaussian	
		Core	Wing
$z_{[\text{C II}]}$	$6.7230 \pm 0.0003$	$6.7224 \pm 0.0003$	$6.7336 \pm 0.0009$
$\text{FWHM}_{[\text{C II}]} \text{ (km s}^{-1}\text{)}$	$536 \pm 26$	$442 \pm 33$	$232 \pm 72$
$S_{[\text{C II}]} \Delta V \text{ (Jy km s}^{-1}\text{)}$	$1.69 \pm 0.07$	$1.49 \pm 0.10$	$0.21 \pm 0.07$
$L_{[\text{C II}]} \text{ (} 10^8 L_{\odot}\text{)}$	$18.7 \pm 0.8$	$16.5 \pm 1.0$	$2.4 \pm 0.8$
$\text{SFR}_{[\text{C II}]} \text{ (} M_{\odot} \text{ yr}^{-1}\text{)}$	$122 \pm 5$	$108 \pm 7$	$16 \pm 6$
Size (beam-convolved)	$(1''.55 \pm 0''.30) \times (1''.03 \pm 0''.17) = (8.3 \pm 1.6) \text{ kpc} \times (5.5 \pm 0.9) \text{ kpc}$		
Size (beam-deconvolved)	$(1''.43 \pm 0''.36) \times (0''.77 \pm 0''.33) = (7.7 \pm 1.9) \text{ kpc} \times (4.1 \pm 1.8) \text{ kpc}$		
	[C II] 158 $\mu$ m Line Emission at Selected Positions (Figure 1)		
	A	B	C
Line center (km s <sup>−1</sup> )	$-49 \pm 54$	$235 \pm 61$	$151 \pm 69$
$\text{FWHM}_{[\text{C II}]} \text{ (km s}^{-1}\text{)}$	$746 \pm 124$	$625 \pm 145$	$775 \pm 162$
$S_{[\text{C II}]} \Delta V \text{ (Jy beam}^{-1} \text{ km s}^{-1}\text{)}$	$0.34 \pm 0.05$	$0.22 \pm 0.04$	$0.27 \pm 0.05$
$L_{[\text{C II}]} \text{ (} 10^8 L_{\odot}\text{)}$	$3.8 \pm 0.6$	$2.5 \pm 0.5$	$3.0 \pm 0.6$
	Continuum Emission ( $T_d = 47$ K, $\beta = 1.6$ , $\kappa_{250 \text{ GHz}} = 0.4 \text{ cm}^2 \text{ g}^{-1}$ )		
$f_{1.2 \text{ mm}} \text{ (mJy)}$	$1.17 \pm 0.04$		
$L_{\text{FIR}} \text{ (} 10^{12} L_{\odot}\text{)}$	$2.7 \pm 0.1$		
$L_{\text{TIR}} \text{ (} 10^{12} L_{\odot}\text{)}$	$3.9 \pm 0.1$		
$\text{SFR}_{\text{TIR}} \text{ (} M_{\odot} \text{ yr}^{-1}\text{)}$	$575 \pm 21$		
$M_{\text{dust}} \text{ (} 10^8 M_{\odot}\text{)}$	$2.0 \pm 0.1$		
Size (beam-convolved)	$(0''.79 \pm 0''.02) \times (0''.52 \pm 0''.01) = (4.3 \pm 0.1) \text{ kpc} \times (2.8 \pm 0.1) \text{ kpc}$		
Size (beam-deconvolved)	$(0''.25 \pm 0''.06) \times (0''.17 \pm 0''.09) = (1.3 \pm 0.3) \text{ kpc} \times (0.9 \pm 0.5) \text{ kpc}$		

**Note.**  $\text{SFR}_{[\text{C II}]}$  for the wing component is appropriate if this reflects a star-forming companion galaxy.

### 3.1. FIR Continuum Properties

The continuum emission ( $\lambda_{\text{obs}} = 1.2$  mm) comes from the central  $\sim 1''$  (see Table 1 for the detailed sizes measured with the CASA task `imfit`). The continuum peaks at (R.A., decl.)<sub>ICRS</sub> = (12<sup>h</sup>05<sup>m</sup>05<sup>s</sup>.080,  $-00^{\circ}00'28''.04$ ), which is consistent with the optical quasar position. To include all extended emission, we measured the continuum flux density with a  $2''$  diameter circular aperture placed at this peak position, resulting in  $f_{1.2 \text{ mm}} = 1.17 \pm 0.04$  mJy.

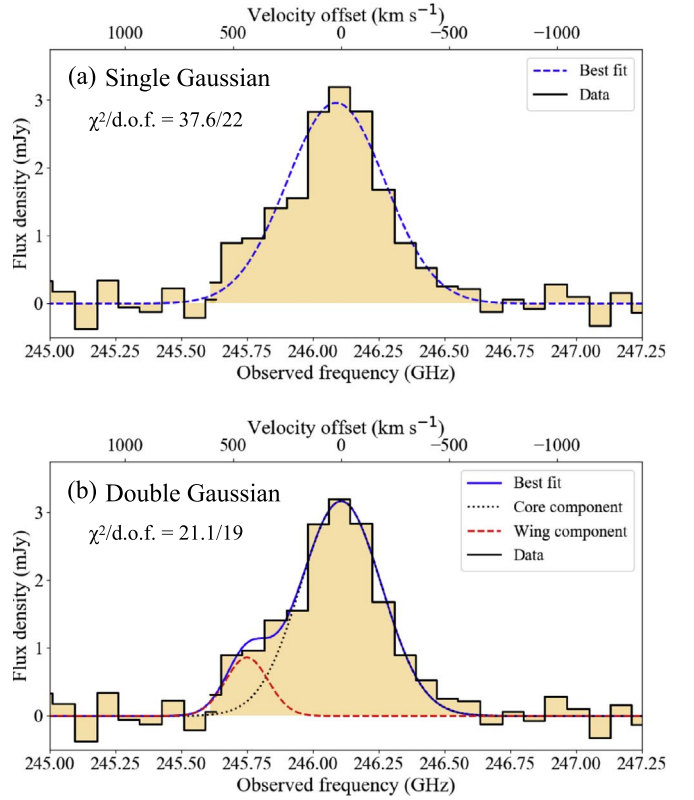
We determined the FIR luminosity ( $L_{\text{FIR}}$ ; 42.5–122.5  $\mu\text{m}$ ) and the total infrared luminosity ( $L_{\text{TIR}}$ ; 8–1000  $\mu\text{m}$ ) by assuming an optically thin modified blackbody with a dust temperature  $T_{\text{d}} = 47$  K and an emissivity index  $\beta = 1.6$ , values that are characteristic of high-redshift luminous quasars (Beelen et al. 2006) and are commonly adopted in the literature (e.g., Izumi et al. 2018). After correcting for contrast and additional heating effects of cosmic microwave background radiation (da Cunha et al. 2013), we obtained  $L_{\text{FIR}} = (2.7 \pm 0.1) \times 10^{12} L_{\odot}$  and  $L_{\text{TIR}} = (3.9 \pm 0.1) \times 10^{12} L_{\odot}$ , respectively. Note that there is actually a wide variation in  $T_{\text{d}}$  from source to source (Venemans et al. 2018). If we adopt  $T_{\text{d}} = 35$  K, typical for local star-forming galaxies (U et al. 2012), these values are roughly halved.

With this  $L_{\text{TIR}}$  ( $T_{\text{d}} = 47$  K) and the calibration of Murphy et al. (2011), we found an SFR of  $575 \pm 21 M_{\odot} \text{ yr}^{-1}$ . However, this should be regarded as an upper limit, as we assumed that the FIR emission is due entirely to star formation, even though there may be a significant contribution from the AGN itself (e.g., Symeonidis 2017). Similarly, by adopting a rest-frame mass absorption coefficient of  $\kappa_{\nu} = 0.4 (\nu/250 \text{ GHz})^{\beta} \text{ cm}^2 \text{ g}^{-1}$  (Alton et al. 2004), we found a dust mass of  $M_{\text{dust}} = (2.0 \pm 0.1) \times 10^8 M_{\odot}$ .

### 3.2. [C II] Line Emission

Figure 1 demonstrates that the [C II] emission is spatially more extended than the FIR continuum emission, extending to  $r \sim 1''$  (5.4 kpc),<sup>33</sup> and has a complex morphology. The extended structure that is directly connected to the continuum-bright core region is real, as we see positive signals from several contiguous velocity channels measured there (Figure 1; positions A–C), over  $[-500, +500] \text{ km s}^{-1}$  relative to the systemic velocity (defined in the following).

Figure 3 shows an area-integrated spectrum measured over the region within a  $1''.5$  radius of the nucleus in which [C II] integrated intensity is detected at more than  $3\sigma$ . We first fit the spectrum with a single Gaussian function (Figure 3(a)), but the observed profile clearly deviates from this model; we found  $\chi^2/\text{degree of freedom (dof)} = 37.6/22$  (estimated over a  $\pm 1200 \text{ km s}^{-1}$  range) for this single Gaussian fit. A notable deviation can be found at positive velocity channels of  $\sim 300$ – $500 \text{ km s}^{-1}$ . As the spatially extended regions (Figure 2) have such high positive velocities, they must contribute to this excess wing of the area-integrated spectrum. We then performed a double Gaussian fit (Figure 3(b)) to account for that excess. This works fairly well with a returned  $\chi^2/\text{dof} = 21.1/19$ . With this difference in  $\chi^2$ , this model is preferred at  $>99.9\%$  confidence. Note that we also see extended [C II] emission in negative velocity channels (Figure 2), but deeper observations are required to confirm its existence (or another wing at the bluer side of the area-integrated spectrum).



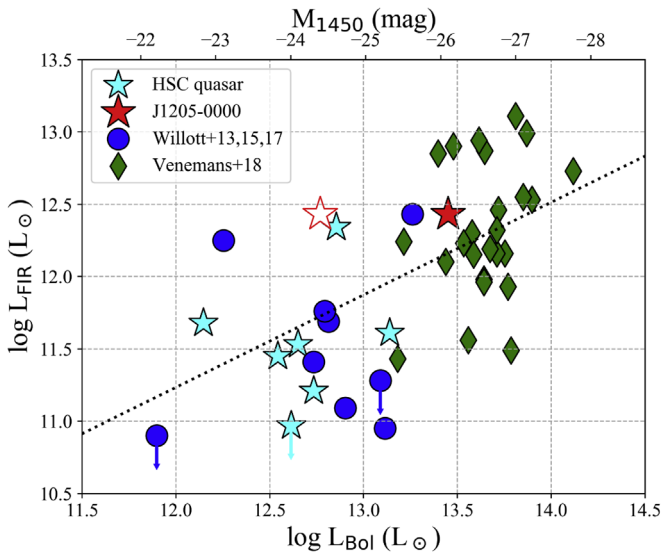
**Figure 3.** Area-integrated [C II] 158  $\mu\text{m}$  spectrum of J1205–0000 measured over a region of [C II] integrated intensity  $>3\sigma \cap r < 1''.5$ . The channel-based sensitivity is 0.21 mJy. (a) Single Gaussian fit and (b) double Gaussian fit to the observed spectrum.

We naively attribute the core component in the double Gaussian fit to the host galaxy itself, hence providing its systemic redshift as  $z_{[\text{C II}]} = 6.7224 \pm 0.0003$ . With respect to this  $z_{[\text{C II}]}$ , Mg II emission ( $z_{\text{Mg II}} = 6.699^{0.007}_{-0.001}$ ; Onoue et al. 2019) is blueshifted by  $-1040^{+310}_{-50} \text{ km s}^{-1}$ . In addition, an absorption feature of a higher ionization line C IV of J1205–0000 is further blueshifted by  $\sim 2900$ – $7400 \text{ km s}^{-1}$  relative to Mg II (Onoue et al. 2019); hence C IV is blueshifted up to  $\sim 8500 \text{ km s}^{-1}$  relative to  $z_{[\text{C II}]}$ . These clearly manifest the existence of very fast nuclear outflows in this red quasar.

With the [C II] core flux and the 1.2 mm continuum flux density (Table 1), we also measured a rest-frame [C II] equivalent width  $\text{EW}_{[\text{C II}]} = 0.67 \pm 0.05 \mu\text{m}$ . This is roughly half of the mean  $\text{EW}_{[\text{C II}]}$  of local star-forming galaxies ( $1.27 \pm 0.53 \mu\text{m}$ ; e.g., Díaz-Santos et al. 2013). In optically low-luminosity  $z > 6$  quasars (e.g., HSC quasars with  $M_{1450} > -25$  mag)  $\text{EW}_{[\text{C II}]}$  is usually  $>1 \mu\text{m}$ , but optically luminous quasars tend to show  $\text{EW}_{[\text{C II}]} < 1 \mu\text{m}$  (Izumi et al. 2019), which is consistent with the intrinsically luminous nature of J1205–0000 ( $M_{1450} = -26.1$  mag after extinction correction; Kato et al. 2020).

Lastly, we estimate the SFR from the [C II] luminosity of this component (Table 1), giving  $108 \pm 7 M_{\odot} \text{ yr}^{-1}$  with the De Looze et al. (2011) calibration, which has  $\sim 0.3$  dex dispersion. Again, this would be an upper limit, as some of the [C II] emission may be due to the quasar itself (i.e., narrow line region). Indeed,  $L_{[\text{C II}]}$  shows a marginal correlation with AGN power (Izumi et al. 2019).

<sup>33</sup> Although the distribution is complex, we fit a two-dimensional elliptical Gaussian to it (CASA task `imfit`; Table 1). The estimated beam-deconvolved size is  $\sim 7.7 \times 4.1 \text{ kpc}^2$ , which is much larger than that of the FIR continuum.



**Figure 4.** Quasar bolometric luminosity ( $L_{\text{Bol}}$ ) vs. FIR continuum luminosity ( $L_{\text{FIR}}$ ) relationship for  $z \gtrsim 6$  quasars. The corresponding  $M_{1450}$  is also shown. Literature data of some optically luminous quasars (Venemans et al. 2018), as well as low-luminosity quasars (Willott et al. 2013, 2015, 2017), including our HSC quasars (Izumi et al. 2018, 2019), are shown. J1205–0000 after (before) extinction correction is indicated by a red filled (open) star. The diagonal line shows our linear regression fit to these objects excluding those with upper limits on  $L_{\text{FIR}}$ .

### 3.3. Comparison to Other $z \gtrsim 6$ Quasars

We briefly compare the quasar nuclear bolometric luminosity ( $L_{\text{Bol}}$ ) and  $L_{\text{FIR}}$  of a sample of  $z \gtrsim 6$  quasars in Figure 4. Here we adopt a bolometric correction factor of 4.4 from 1450 Å luminosity (Richards et al. 2006) to compute  $L_{\text{Bol}}$ . The same assumptions presented in Section 3.1 are made to derive  $L_{\text{FIR}}$ . Optically luminous quasar data is compiled from a recent survey work of Venemans et al. (2018), whereas we collected the data of relatively low-luminosity quasars from Willott et al. (2013, 2015, 2017) and Izumi et al. (2018, 2019).

Although there is admittedly a wide spread in  $L_{\text{FIR}}$  for a given  $L_{\text{Bol}}$ , J1205–0000 shows a characteristic  $L_{\text{FIR}}$  to the optically luminous quasars once its dust extinction is corrected. If we assume that a quasar-phase happens during a longer-timescale starburst phase (e.g., Davies et al. 2007; Hopkins et al. 2008; Bergvall et al. 2016), there was once a growing obscured AGN phase in J1205–0000 that was embedded in this starburst host galaxy.

At the lower quasar luminosity regime, i.e.,  $L_{\text{Bol}} < 10^{13} L_{\odot}$ , there are only two quasars (out of 12) having comparable  $L_{\text{FIR}}$  to J1205–0000, namely J2239+0207 (Izumi et al. 2019) and VIMOS 2911 (Willott et al. 2017). J2239+0207 is likely to have a close [C II] companion galaxy, which may have triggered its intense starburst (Izumi et al. 2019). VIMOS 2911, which was originally discovered by Kashikawa et al. (2015), seems to be an outlier in this plane as no companion has been reported (Willott et al. 2017), and its narrow [C II] line profile (FWHM = 264 km s<sup>-1</sup>) indicates the absence of a merger-like active event. The remaining low-luminosity quasars all show  $L_{\text{FIR}} < 10^{12} L_{\odot}$  (some show as low as  $< 10^{11} L_{\odot}$ ), which is clearly not the case for the optically luminous quasars.

Indeed, we found a positive correlation between  $\log L_{\text{Bol}}$  and  $\log L_{\text{FIR}}$ , after excluding the objects with upper limits on  $L_{\text{FIR}}$ ,

as follows:

$$\log \left( \frac{L_{\text{FIR}}}{L_{\odot}} \right) = (0.64 \pm 0.03) \times \log \left( \frac{L_{\text{Bol}}}{L_{\odot}} \right) + (3.55 \pm 0.45). \quad (1)$$

The Spearman correlation coefficient for this  $\log L_{\text{Bol}} - \log L_{\text{FIR}}$  data is 0.56 ( $p$ -value =  $2.0 \times 10^{-4}$ ). Although it is still a marginal correlation, this implies that a black hole and its host galaxy are actually coevolving at this high redshift. In addition, if we assume a common star formation efficiency over the whole quasars used here, this correlation suggests that an optically luminous quasar tends to form in a gas-richer galaxy. Note that Venemans et al. (2018) did not find a significant correlation between these two luminosities, likely because they only studied optically luminous quasars.

## 4. Nature of the Extended [C II] Emission

We now turn to the physical origin of the extended [C II] structure, which also contributes to the [C II] wing in the area-integrated spectrum. Major possibilities include a companion/merging galaxy and cold outflow. However, as detailed later, it is not possible to distinguish these two scenarios with the current data set. Thus, we discuss both of these scenarios and provide relevant properties in the following. Note that other key properties, including the early coevolution of this quasar, will be discussed in our forthcoming paper, along with those of the other HSC quasars observed in our ALMA Cycle 7 program (T. Izumi et al. 2021, in preparation).

### 4.1. Companion/Merging Galaxies?

Major mergers of gas-rich galaxies have been considered to be a promising driver of quasar activity (e.g., Sanders et al. 1988; Di Matteo et al. 2005; Hopkins et al. 2006). High-resolution and/or high-sensitivity observations at the low-redshift universe indeed show an enhanced AGN fraction in major merger systems (e.g., Ellison et al. 2011; Silverman et al. 2011; Goulding et al. 2018; Koss et al. 2018). It is also noteworthy that (the intrinsically luminous) red quasars tend to be hosted by major merger systems (e.g., Urrutia et al. 2008; Glikman et al. 2015). In this context, it is intriguing that recent sensitive ALMA observations of rest-FIR continuum and/or [C II] emission have started to uncover star-forming companion galaxies to some  $z \gtrsim 5$ –6 luminous quasars (e.g., Wang et al. 2011; Decarli et al. 2017; Trakhtenbrot et al. 2017; Willott et al. 2017; Neeleman et al. 2019), with some of these companions very close to, or even merging with, the main quasar (Bañados et al. 2019; Decarli et al. 2019; Venemans et al. 2019, 2020).

We found that the [C II] spatial distribution of J1205–0000, including the channel maps (Figures 1 and 2), well resembles that of J1342+0928 at  $z = 7.54$  (Bañados et al. 2019), which is considered to be an ongoing merger system. Therefore it is plausible that the extended [C II] structure of J1205–0000 is due to very close companion or merging galaxies. As the [C II] emission extends toward multiple directions, there could be corresponding multiple mergers in J1205–0000. This picture fits into an evolutionary scenario in which a red quasar corresponds to an emergent phase from a merger-induced dusty starburst. A high fraction of merger events in red quasar–host galaxies (e.g., Urrutia et al. 2008; Glikman et al. 2015) measured at lower redshifts also supports this scenario. Although we need higher-resolution and

**Table 2**  
Possible Galaxy-scale [C II] Outflow Properties of J1205–0000

Blob ID	$v_{\text{out}}$ ( $\text{km s}^{-1}$ )	$M_{\text{out}}$ ( $10^8 M_{\odot}$ )	$\tau_{\text{out}}$ ( $10^7 \text{ yr}$ )	$\dot{M}_{\text{out}}$ ( $M_{\odot} \text{ yr}^{-1}$ )	$\dot{E}_{\text{out}}$ ( $10^8 L_{\odot}$ )	$\dot{P}_{\text{out}}/\dot{P}_{\text{AGN}}$ (%)
A	$422 \pm 82$	$3.8 \pm 0.6$	$0.8 \pm 0.2$	$45 \pm 11$	$6.6 \pm 2.4$	$4.3 \pm 1.4$
B	$547 \pm 95$	$2.4 \pm 0.5$	$1.1 \pm 0.2$	$21 \pm 5$	$5.1 \pm 1.8$	$2.6 \pm 0.8$
C	$538 \pm 106$	$2.9 \pm 0.5$	$0.9 \pm 0.2$	$31 \pm 8$	$7.5 \pm 2.9$	$3.9 \pm 1.3$

higher-sensitivity [C II] data to better understand the dynamical nature of this system, J1205–0000 has great potential to be an ideal laboratory in which to study the physical properties of merging galaxies that would eventually evolve into unobscured luminous quasars.

Note that we did not find any companion in our optical  $z$ - and  $y$ -band maps ( $\sim 0''.8$  resolution) with  $5\sigma$  limiting magnitudes of  $(z_{\text{AB}}, y_{\text{AB}}) = (25.1, 24.4)$ , taken by the HSC (Matsuoka et al. 2016; see also Figure 1). Although previous ALMA observations actually uncovered optically unidentified [C II] or FIR continuum emitters around some  $z > 6$  quasars (e.g., Decarli et al. 2017; Mazzucchelli et al. 2019), the situation appears to be different in J1205–0000. Those known companions are typically bright at FIR with  $\text{SFR}_{\text{IR}}$  of  $> 100 M_{\odot} \text{ yr}^{-1}$ . Hence their stellar emission would suffer severe dust extinction, which can make them optically unidentifiable (Mazzucchelli et al. 2019). In contrast to this, the FIR continuum emission of J1205–0000 is undetected ( $< 1.5\sigma$ ) at regions with spatially extended [C II] emission (Figure 1). An inferred  $3\sigma$  upper limit on  $\text{SFR}_{\text{IR}}$  by assuming a modest  $T_{\text{d}}$  of 35 K (the typical value of local star-forming galaxies; U et al. 2012) is only  $\sim 10 M_{\odot} \text{ yr}^{-1}$ . Hence the corresponding dust extinction is not so significant for the potential companions of J1205–0000. Rather, an insufficient optical survey depth would simply have been the cause. If we suppose Lyman-break galaxies (LBGs) are responsible for the potential companions, our  $y$ -band observation ( $5\sigma_{\text{AB}} = 24.4$  mag) only probes the bright end of the UV luminosity function of LBGs at  $z \sim 7$  (Ono et al. 2018). In this regard, much deeper data from future facilities such as the James Webb Space Telescope (JWST) is needed to conclusively identify the companions.

#### 4.2. Cold Neutral Outflows?

The extended and complex gas morphology of J1205–0000 also reminds us of the morphology of J1148+5251, the only other known  $z > 6$  quasar with prominent [C II] outflows. While J1148+5251 is around five times as bright as J1205–0000 at UV and the observed [C II] extent is as large as  $r \sim 30$  kpc (Cicone et al. 2015), this hints at the existence of cold outflows in J1205–0000 as well. In addition, the off-center [C II] spectra are all broad ( $\text{FWHM} \gtrsim 600\text{--}800 \text{ km s}^{-1}$ ). These are even broader than those of the core component, as well as those of known companion galaxies of  $z > 6$  quasars ( $\lesssim 400\text{--}500 \text{ km s}^{-1}$ ; e.g., Neeleman et al. 2019), which would prefer the outflow scenario. Thus, we discuss potential outflow properties hereafter by assuming that the extended structure is formed fully due to cold outflows. Given that the (potential) outflows are both spatially and spectrally resolved, we can measure the dynamical timescales of each [C II] blob defined in Figure 1 (A, B, C). With these timescales, we follow the standard prescription (e.g., Bischetti et al. 2019) to estimate the outflow rate, kinetic power, and momentum (Table 2).

We define the outflow rate as  $\dot{M}_{\text{out}} = M_{\text{out}} v_{\text{out}} / R_{\text{out}}$ , where  $M_{\text{out}}$  is the outflowing mass,  $v_{\text{out}}$  is the outflow velocity, and  $R_{\text{out}}$  is the distance from the continuum peak. For  $v_{\text{out}}$ , we adopt  $|\Delta v| + \text{FWHM}/2$ , which combines the shift of the velocity centroid from the systemic redshift and the FWHM of each blob.  $R_{\text{out}}$  is directly measured from Figure 1 as 3.5, 6.4, and 5.1 kpc for blobs A–C, respectively. Note that  $v_{\text{out}}$  is projected along the line of sight, and  $R_{\text{out}}$  is projected in the plane of the sky; thus,  $\tau_{\text{out}}$  should be corrected by a factor of  $|\tan \alpha|^{-1}$ , where  $\alpha$  is the angle between our line of sight and the outflow direction of each blob. While we do not know  $\alpha$  a priori, the average of this factor over all angles is unity.

We calculate the outflow mass in neutral hydrogen gas  $M_{\text{out}}$  as

$$\frac{M_{\text{out}}}{M_{\odot}} = 0.77 \left( \frac{0.7 L_{[\text{C II}]}}{L_{\odot}} \right) \left( \frac{1.4 \times 10^{-4}}{X_{\text{C}^+}} \right) \times \frac{1 + 2e^{-91/T_{\text{ex}}} + n_{\text{crit}}/n}{2e^{-91/T_{\text{ex}}}}, \quad (2)$$

where  $X_{\text{C}^+}$  is the  $\text{C}^+$  fraction per H atom,  $T_{\text{ex}}$  is the excitation temperature in kelvin,  $n$  is the gas density, and  $n_{\text{crit}}$  is the line critical density ( $\sim 3 \times 10^3 \text{ cm}^{-3}$ ). As the actual gas density is unknown, we here assume the high-density limit ( $n \gg n_{\text{crit}}$ ) to provide a lower limit on  $M_{\text{out}}$ . The factor 0.7 in the first parenthesis indicates the typical fraction of [C II] arising from photodissociation regions (PDRs; i.e., the remaining 30% originates from H II regions). For consistency with previous works (e.g., Maiolino et al. 2012; Cicone et al. 2015), we adopt  $X_{\text{C}^+} = 1.4 \times 10^{-4}$  and  $T_{\text{ex}} = 200$  K, which are characteristic of PDRs (e.g., Hollenbach & Tielens 1997), but varying  $T_{\text{ex}} \in [100, 1000]$  K changes the inferred  $M_{\text{out}}$  by only  $\sim 20\%$ .

Interestingly, the (projected) flow times of blobs A–C are all clustered around  $\sim 10^7$  yr, which suggests that these outflows were launched at roughly the same time. Summing over these three blobs, the total atomic outflow mass and outflow rate are  $M_{\text{out,A-C}} = 9.0 \pm 0.9 \times 10^8 M_{\odot}$  and  $\dot{M}_{\text{out,A-C}} = 97 \pm 15 M_{\odot} \text{ yr}^{-1}$ , respectively. The summed outflow rate is around eight times as high as the (current) black hole accretion rate of J1205–0000 ( $\dot{M}_{\text{BH}} \sim 12.5 M_{\odot} \text{ yr}^{-1}$ ), which is estimated from the quasar bolometric luminosity ( $L_{\text{AGN}} = 8.3 \times 10^{46} \text{ erg s}^{-1}$ ; Kato et al. 2020) with a canonical radiative efficiency of  $\varepsilon = 0.1$ .

Note, however, that our (possible) outflow rate only refers to the neutral atomic component, while a significant fraction of the outflowing gas would be in a molecular phase. Indeed, Fluetsch et al. (2019) found in local galaxies that the total mass-flow rate is  $\sim 0.5$  dex higher than the atom-only value. As our computation provided a lower limit on  $M_{\text{out}}$  and we measured rates only at the three selected positions, J1205–0000 is likely to have a (possible) total outflow rate of  $\dot{M}_{\text{tot}} \gtrsim 300 M_{\odot} \text{ yr}^{-1}$ . This is a factor of  $\gtrsim 3$  greater than the [C II]-based SFR, and it is not typical for star

formation to drive a wind at a much greater rate than the SFR (e.g., Ciccone et al. 2014). We therefore naively suppose that the quasar itself powers this outflow. We emphasize that J1205–0000 is the highest-redshift red quasar known to date. Therefore, it is intriguing that the existence of outflows on the scale of the host galaxy is hinted at here, suggesting that the surrounding interstellar medium is actively being blown out, as predicted in SMBH/galaxy evolution scenarios (e.g., Hopkins et al. 2006).

We found that the peak flux density of the red wing is  $\sim 30\%$  of that of the core component, while Maiolino et al. (2012) found a broad-to-narrow peak flux density ratio of  $\sim 15\%$  for the case of J1148+5251. The (possible) outflow velocity is much lower in J1205–0000 than in J1148+5251, but we may be limited by the sensitivity of our measurement to detecting faster components. Interestingly, a similar line profile to J1205–0000 is seen in cold outflows of lower-redshift obscured quasars (e.g., Brusa et al. 2018; Fan et al. 2018). Hence suppose that the high-peak wing is due to a dense gas that once obscured the nucleus in a shell-like form. It had a high wind velocity when it was launched, but is now decelerating after traveling a long way from the center. As time progresses and the quasar becomes less reddened, the outflow will continue to slow down. It would be hard to identify such a low-velocity component as an outflow unless it is spatially resolved. Indeed, spatially extended but low-velocity ( $|\Delta v| < 200 \text{ km s}^{-1}$ ) structures are also found in J1148+5251 (Ciccone et al. 2015).

If the extended structures were formed genuinely due to outflows, both the outflow kinetic power

$$\dot{E}_{\text{out}} = \frac{1}{2} \dot{M}_{\text{out}} v_{\text{out}}^2 \quad (3)$$

and the momentum load

$$\dot{P}_{\text{out}}/\dot{P}_{\text{AGN}} = \frac{\dot{M}_{\text{out}} \times v_{\text{out}}}{L_{\text{AGN}}/c} \quad (4)$$

are significantly smaller (Table 2) than what energy-conserving AGN feedback models typically predict ( $\dot{E}_{\text{out}} \sim 0.05 \times L_{\text{AGN}}$ ,  $\dot{P}_{\text{out}}/\dot{P}_{\text{AGN}} \sim 20$ ; e.g., King & Pounds 2015). The small values found here are comparable to those of J1148+5251 (Ciccone et al. 2015), implying that these may be typical among both red and blue  $z \gtrsim 6$  quasars. Hence, the nuclear winds contribute only a small fraction of galaxy-scale feedback if we apply this energy-conserving feedback scenario. This indicates that, without additional feedback from star formation, AGN feedback is not able to completely suppress star formation over the entire host galaxy.

## 5. Summary

We have presented ALMA observations of [C II] line and underlying FIR continuum emission of the highest-redshift red quasar known to date, J1205–0000 at  $z = 6.72$ , which was discovered in our deep optical imaging survey with the Subaru HSC. Although it appears as a low-luminosity quasar ( $M_{1450} = -24.4 \text{ mag}$ ), its intrinsic luminosity is as high as  $M_{1450} = -26.1 \text{ mag}$  once its dust extinction is corrected. A red quasar population has been considered as an emergent phase from a dusty starburst blowing out its surrounding dense obscuring medium. The main findings of this paper are summarized as follows.

1. We successfully detected [C II] line and FIR continuum emission. The [C II] emission is spatially more extended (over  $r \sim 5 \text{ kpc}$  scale) than the continuum emission. The area-integrated [C II] line profile is complex and is characterized by two components, i.e., a main core component that is attributed to the host galaxy itself and an additional red wing component. Summing up these two, we found a line luminosity of  $L_{[\text{C II}]} = (1.9 \pm 0.1) \times 10^9 L_{\odot}$ . The FIR continuum emission is also bright:  $L_{\text{FIR}} = (2.7 \pm 0.1) \times 10^{12} L_{\odot}$  ( $T_d = 47 \text{ K}$ ,  $\beta = 1.6$ ).
2. The SFR inferred from the continuum luminosity and [C II] core luminosity is  $575 \pm 21 M_{\odot} \text{ yr}^{-1}$  and  $108 \pm 7 M_{\odot} \text{ yr}^{-1}$ , respectively. Note, however, that these would be regarded as upper limits as we neglected contamination from this intrinsically luminous quasar itself.
3. Based on the [C II] equivalent width and  $L_{\text{Bol}}-L_{\text{FIR}}$  relation, we found that J1205–0000 shows properties consistent with  $z \gtrsim 6$  optically luminous quasars once its dust extinction is corrected. We also found a marginal positive correlation between  $L_{\text{Bol}}$  and  $L_{\text{FIR}}$ , implying a black hole and its host galaxy are coevolving.
4. Although it is not practical to identify the physical origin of the spatially extended [C II] emission with the current data set, possible explanations include (i) companion/merging galaxies and (ii) cold outflows. Both of these are fascinating as they closely fit the merger-induced galaxy evolution scenario.
5. If the extended structure is due to (multiple) companion/merging galaxies, this indicates that this red quasar indeed emerges with a merger event. While no counterpart was identified in our optical imaging survey with the Subaru HSC (e.g.,  $y$ -band  $5\sigma$  limiting magnitude = 24.4 mag), dust extinction would not be the prime cause of this given the nondetection of FIR continuum emission. Rather, our observations may still be not sensitive enough to detect normal galaxies like LBGs at that high redshift. Deeper imaging observations by future facilities like JWST are necessary to search for possible companion/merging galaxies.
6. If the extended structure is due to cold outflows, we can argue that this red quasar is in a key transition phase from a dusty starburst blowing out its surrounding medium. On the other hand, our lower limit on the cold neutral outflow is only  $\sim 100 M_{\odot} \text{ yr}^{-1}$ , and we found that the outflow kinetic energy and momentum are both much lower than predicted in energy-conserving wind models. This suggests that the AGN feedback in this quasar, if it genuinely exists, is not sufficient to suppress star formation of the host galaxy.

In this work, we have revealed some intriguing host galaxy properties of this red quasar. This red quasar was originally identified by matching our low-luminosity quasar sample and the mid-infrared photometric data obtained by WISE (Kato et al. 2020). As the HSC survey is still ongoing and our sample of  $z = 6-7$  low-luminosity quasars has been growing, we will be able to find other red quasars at this high redshift. They should be a good sample for extensive follow-up studies by, e.g., ALMA and JWST, to better understand early black hole growth and coevolution.



We appreciate the anonymous referee's thorough reading and very constructive comments, which improved this paper greatly. This paper makes use of the following ALMA data: ADS/JAO.ALMA#2019.1.00074.S. ALMA is a partnership of the ESO (representing its member states), the NSF (USA), and NINS (Japan), together with NRC (Canada), the MOST and the ASIAA (Taiwan), and KASI (Republic of Korea), in cooperation with the Republic of Chile. The Joint ALMA Observatory is operated by ESO, AUI/NRAO, and NAOJ.

The HSC Collaboration includes the astronomical communities of Japan and Taiwan and Princeton University. The HSC instrumentation and software were developed by NAOJ, the Kavli Institute for the Physics and Mathematics of the Universe (Kavli IPMU), the University of Tokyo, the High Energy Accelerator Research Organization (KEK), ASIAA, and Princeton University. Funding was contributed by the FIRST program of the Japanese Cabinet Office, the Ministry of Education, Culture, Sports, Science, and Technology, the Japan Society for the Promotion of Science, the Japan Science and Technology Agency, the Toray Science Foundation, NAOJ, Kavli IPMU, KEK, ASIAA, and Princeton University.

T.I. is supported by an ALMA Japan Research Grant of the NAOJ ALMA Project, NAOJ-ALMA-249.

*Software:* CASA (McMullin et al. 2007), MIRIAD (Sault et al. 1995), astropy (Astropy Collaboration et al. 2013, 2018).

### ORCID iDs

Takuma Izumi  <https://orcid.org/0000-0001-9452-0813>  
 Masafusa Onoue  <https://orcid.org/0000-0003-2984-6803>  
 Michael A. Strauss  <https://orcid.org/0000-0002-0106-7755>  
 Seiji Fujimoto  <https://orcid.org/0000-0001-7201-5066>  
 Hideki Umehata  <https://orcid.org/0000-0003-1937-0573>  
 Masatoshi Imanishi  <https://orcid.org/0000-0001-6186-8792>  
 Taiki Kawamuro  <https://orcid.org/0000-0002-6808-2052>  
 Tohru Nagao  <https://orcid.org/0000-0002-7402-5441>  
 Yoshiki Toba  <https://orcid.org/0000-0002-3531-7863>  
 Kotaro Kohno  <https://orcid.org/0000-0002-4052-2394>  
 Nobunari Kashikawa  <https://orcid.org/0000-0003-3954-4219>  
 Kohei Inayoshi  <https://orcid.org/0000-0001-9840-4959>  
 Toshihiro Kawaguchi  <https://orcid.org/0000-0002-3866-9645>  
 Kazushi Iwasawa  <https://orcid.org/0000-0002-4923-3281>  
 Shunsuke Baba  <https://orcid.org/0000-0002-9850-6290>  
 Hyewon Suh  <https://orcid.org/0000-0002-2536-1633>  
 Yuichi Harikane  <https://orcid.org/0000-0002-6047-430X>  
 Yoshihiro Ueda  <https://orcid.org/0000-0001-7821-6715>  
 John D. Silverman  <https://orcid.org/0000-0002-0000-6977>  
 Takuya Hashimoto  <https://orcid.org/0000-0002-0898-4038>  
 Daisuke Iono  <https://orcid.org/0000-0002-2364-0823>  
 Chien-Hsiu Lee  <https://orcid.org/0000-0003-1700-5740>  
 Kianhong Lee  <https://orcid.org/0000-0003-4814-0101>  
 Takeo Minezaki  <https://orcid.org/0000-0002-2933-048X>  
 Kouichiro Nakanishi  <https://orcid.org/0000-0002-6939-0372>  
 Yoichi Tamura  <https://orcid.org/0000-0003-4807-8117>  
 Ji-Jia Tang  <https://orcid.org/0000-0002-1860-0886>

### References

Aihara, H., Arimoto, N., Armstrong, R., et al. 2018, *PASJ*, 70, S4  
 Alton, P. B., Xilouris, E. M., Misiriotis, A., Dasyra, K. M., & Dumke, M. 2004, *A&A*, 425, 109

Astropy Collaboration, Price-Whelan, A. M., SipHocz, B. M., et al. 2018, *AJ*, 156, 123  
 Astropy Collaboration, Robitaille, T. P., Tollerud, E. J., et al. 2013, *A&A*, 558, A33  
 Bañados, E., Novak, M., Neeleman, M., et al. 2019, *ApJL*, 881, L23  
 Bañados, E., Venemans, B. P., Decarli, R., et al. 2016, *ApJS*, 227, 11  
 Beelen, A., Cox, P., Benford, D. J., et al. 2006, *ApJ*, 642, 694  
 Bergvall, N., Marquart, T., Way, M. J., et al. 2016, *A&A*, 587, A72  
 Bischetti, M., Maiolino, R., Carniani, S., et al. 2019, *A&A*, 630, A59  
 Brusa, M., Cresci, G., Daddi, E., et al. 2018, *A&A*, 612, A29  
 Carniani, S., Marconi, A., Maiolino, R., et al. 2016, *A&A*, 591, A28  
 Cicone, C., Maiolino, R., Gallerani, S., et al. 2015, *A&A*, 574, A14  
 Cicone, C., Maiolino, R., Sturm, E., et al. 2014, *A&A*, 562, A21  
 da Cunha, E., Groves, B., Walter, F., et al. 2013, *ApJ*, 766, 13  
 Davies, R. I., Müller Sánchez, F., Genzel, R., et al. 2007, *ApJ*, 671, 1388  
 De Looze, I., Baes, M., Bendo, G. J., Cortese, L., & Fritz, J. 2011, *MNRAS*, 416, 2712  
 Decarli, R., Dotti, M., Bañados, E., et al. 2019, *ApJ*, 880, 157  
 Decarli, R., Walter, F., Venemans, B. P., et al. 2017, *Natur*, 545, 457  
 Decarli, R., Walter, F., Venemans, B. P., et al. 2018, *ApJ*, 854, 97  
 Di Matteo, T., Springel, V., & Hernquist, L. 2005, *Natur*, 433, 604  
 Díaz-Santos, T., Armus, L., Charmandaris, V., et al. 2013, *ApJ*, 774, 68  
 Ellison, S. L., Patton, D. R., Mendel, J. T., & Scudder, J. M. 2011, *MNRAS*, 418, 2043  
 Estrada-Carpenter, V., Papovich, C., Momcheva, I., et al. 2020, *ApJ*, 898, 171  
 Fan, L., Knudsen, K. K., Fogasy, J., & Drouart, G. 2018, *ApJL*, 856, L5  
 Fan, X., Narayanan, V. K., Lupton, R. H., et al. 2001, *AJ*, 122, 2833  
 Farrar, D., Urrutia, T., Lacy, M., et al. 2012, *ApJ*, 745, 178  
 Fluetsch, A., Maiolino, R., Carniani, S., et al. 2019, *MNRAS*, 483, 4586  
 Glikman, E., Gregg, M. D., Lacy, M., et al. 2004, *ApJ*, 607, 60  
 Glikman, E., Lacy, M., LaMassa, S., et al. 2018, *ApJ*, 861, 37  
 Glikman, E., Simmons, B., Mailly, M., et al. 2015, *ApJ*, 806, 218  
 Goulding, A. D., Greene, J. E., Bezanson, R., et al. 2018, *PASJ*, 70, S37  
 Hickox, R. C., & Alexander, D. M. 2018, *ARA&A*, 56, 625  
 Hollenbach, D. J., & Tielens, A. G. G. M. 1997, *ARA&A*, 35, 179  
 Hopkins, P. F., Hernquist, L., Cox, T. J., et al. 2006, *ApJS*, 163, 1  
 Hopkins, P. F., Hernquist, L., Cox, T. J., & Kereš, D. 2008, *ApJS*, 175, 356  
 Inayoshi, K., Visbal, E., & Haiman, Z. 2020, *ARA&A*, 58, 27  
 Izumi, T., Onoue, M., Matsuoka, Y., et al. 2019, *PASJ*, 71, 111  
 Izumi, T., Onoue, M., Shirakata, H., et al. 2018, *PASJ*, 70, 36  
 Kashikawa, N., Ishizaki, Y., Willott, C. J., et al. 2015, *ApJ*, 798, 28  
 Kato, N., Matsuoka, Y., Onoue, M., et al. 2020, *PASJ*, 72, 84  
 King, A., & Pounds, K. 2015, *ARA&A*, 53, 115  
 Kormendy, J., & Ho, L. C. 2013, *ARA&A*, 51, 511  
 Koss, M. J., Blecha, L., Bernhard, P., et al. 2018, *Natur*, 563, 214  
 Lutz, D., Sturm, E., Janssen, A., et al. 2020, *A&A*, 633, A134  
 Maiolino, R., Gallerani, S., Neri, R., et al. 2012, *MNRAS*, 425, L66  
 Marshall, M. A., Mutch, S. J., Qin, Y., Poole, G. B., & Wyithe, J. S. B. 2020, *MNRAS*, 494, 2747  
 Matsuoka, Y., Iwasawa, K., Onoue, M., et al. 2018a, *ApJS*, 237, 5  
 Matsuoka, Y., Onoue, M., Kashikawa, N., et al. 2016, *ApJ*, 828, 26  
 Matsuoka, Y., Onoue, M., Kashikawa, N., et al. 2018b, *PASJ*, 70, S35  
 Mazzucchelli, C., Bañados, E., Venemans, B. P., et al. 2017, *ApJ*, 849, 91  
 Mazzucchelli, C., Decarli, R., Farina, E. P., et al. 2019, *ApJ*, 881, 163  
 McMullin, J. P., Waters, B., Schiebel, D., Young, W., & Golap, K. 2007, in ASP Conf. Ser. 376, *Astronomical Data Analysis Software and Systems XVI*, ed. R. A. Shaw, F. Hill, & D. J. Bell (San Francisco, CA: ASP), 127  
 Murphy, E. J., Condon, J. J., Schinnerer, E., et al. 2011, *ApJ*, 737, 67  
 Neeleman, M., Bañados, E., Walter, F., et al. 2019, *ApJ*, 882, 10  
 Novak, M., Venemans, B. P., Walter, F., et al. 2020, *ApJ*, 904, 131  
 Ono, Y., Ouchi, M., Harikane, Y., et al. 2018, *PASJ*, 70, S10  
 Onoue, M., Kashikawa, N., Matsuoka, Y., et al. 2019, *ApJ*, 880, 77  
 Perrotta, S., Hamann, F., Zakamska, N. L., et al. 2019, *MNRAS*, 488, 4126  
 Richards, G. T., Hall, P. B., Vand en Berk, D. E., et al. 2003, *AJ*, 126, 1131  
 Richards, G. T., Lacy, M., Storrie-Lombardi, L. J., et al. 2006, *ApJS*, 166, 470  
 Ross, N. P., Hamann, F., Zakamska, N. L., et al. 2015, *MNRAS*, 453, 3932  
 Sanders, D. B., Soifer, B. T., Elias, J. H., et al. 1988, *ApJ*, 325, 74  
 Sault, R. J., Teuben, P. J., & Wright, M. C. H. 1995, in ASP Conf. Ser. 77, *Astronomical Data Analysis Software and Systems IV*, ed. R. A. Shaw, H. E. Payne, & J. J. E. Hayes (San Francisco, CA: ASP), 433, arXiv:astro-ph/0612759  
 Shirakata, H., Okamoto, T., Kawaguchi, T., et al. 2019, *MNRAS*, 482, 4846  
 Silverman, J. D., Kampeczyk, P., Jahnke, K., et al. 2011, *ApJ*, 743, 2  
 Straatman, C. M. S., Labbé, I., Spitler, L. R., et al. 2014, *ApJL*, 783, L14  
 Symeonidis, M. 2017, *MNRAS*, 465, 1401  
 Trakhtenbrot, B., Lira, P., Netzer, H., et al. 2017, *ApJ*, 836, 8

- U, V., Sanders, D. B., Mazzarella, J. M., et al. 2012, [ApJS](#), 203, 9
- Urrutia, T., Becker, R. H., White, R. L., et al. 2009, [ApJ](#), 698, 1095
- Urrutia, T., Lacy, M., & Becker, R. H. 2008, [ApJ](#), 674, 80
- Venemans, B. P., Decarli, R., Walter, F., et al. 2018, [ApJ](#), 866, 159
- Venemans, B. P., Neeleman, M., Walter, F., et al. 2019, [ApJL](#), 874, L30
- Venemans, B. P., Walter, F., Decarli, R., et al. 2017, [ApJ](#), 845, 154
- Venemans, B. P., Walter, F., Neeleman, M., et al. 2020, [ApJ](#), 904, 130
- Venemans, B. P., Walter, F., Zschaechner, L., et al. 2016, [ApJ](#), 816, 37
- Wang, R., Wagg, J., Carilli, C. L., et al. 2011, [ApJL](#), 739, L34
- Wang, R., Wagg, J., Carilli, C. L., et al. 2013, [ApJ](#), 773, 44
- Willott, C. J., Bergeron, J., & Omont, A. 2015, [ApJ](#), 801, 123
- Willott, C. J., Bergeron, J., & Omont, A. 2017, [ApJ](#), 850, 108
- Willott, C. J., Omont, A., & Bergeron, J. 2013, [ApJ](#), 770, 13
- Zakamska, N. L., Sun, A.-L., Strauss, M. A., et al. 2019, [MNRAS](#), 489, 497